Uniform momentum zones in turbulent boundary layers

Charitha M. de Silva[1,†], Nicholas Hutchins[1] and Ivan Marusic[1]

[1]Department of Mechanical Engineering, The University of Melbourne, Victoria 3010, Australia

Structural properties of regions of uniform streamwise momentum in turbulent boundary layers are examined using experimental databases obtained from particle image velocimetry. This investigation employs a large range of Reynolds numbers, spanning more than an order of magnitude ($Re_\tau = 10^3$–10^4), enabling us to provide a detailed description of uniform momentum zones as a function of Reynolds number. Our analysis starts by examining the identification criterion used by Adrian *et al.* (*J. Fluid Mech.*, vol. 422, 2000, pp. 1–54) to report the presence of uniform momentum zones in turbulent boundary layers. This criterion is then applied to show that a zonal-like structural arrangement is prevalent in all datasets examined, emphasising its importance in the structural organisation. Streamwise velocity fluctuations within the zones are observed to be small but they are bounded by distinct step changes in streamwise momentum which indicate that shear layers of intense vorticity separate each zone. A log-linear increase in the number of these zones with increasing Reynolds number is revealed, together with an increase in the thicknesses of zones with increasing distance from the wall. These results support a hierarchical length-scale distribution of coherent structures, which generate zonal-like organisation within turbulent boundary layers. Interpretation of these findings is aided by employing synthetic velocity fields generated using a model based on the attached eddy hypothesis, which is described in the work of Perry and co-workers. Comparisons between the model and experimental results show that a hierarchy of self-similar structures leads to population densities and length-scale distributions of uniform momentum zones that closely adhere to those observed experimentally in this study.

Key words: boundary layer structure, boundary layers, turbulent boundary layers

1. Introduction

The structural nature of turbulent boundary layers has been the subject of many investigations. Over the last half a century, a large number of studies have shown that turbulent boundary layers are populated by a hierarchy of recurrent structures, commonly referred to as 'coherent structures'. These include: low- and high-speed streaks (Kline *et al.* 1967; Offen & Kline 1975), ejection and sweeps (Wallace, Eckelmann & Brodkey 1972), streamwise vortices (Blackwelder & Eckelmann 1979),

† Email address for correspondence: desilvac@unimelb.edu.au

hairpin vortices (Theodersen 1952; Offen & Kline 1974; Head & Bandyopadhyay 1981), large-scale three-dimensional bulges (Falco 1977), packets of hairpin vortices (Head & Bandyopadhyay 1981; Zhou *et al.* 1999; Adrian, Meinhart & Tomkins 2000), very-large-scale motions (Kim & Adrian 1999) and superstructures (Hutchins & Marusic 2007). Significant effort has been put into investigating coherent motions to understand their scaling laws, generation/interaction mechanisms, and their role in the production and dissipation of turbulence (Smits, McKeon & Marusic 2011; Herpin *et al.* 2013). Further efforts have also been made in an attempt to model these structural features, with models based on hairpin or packet-like structures gaining broad interest (summarised recently by Adrian 2007 and Adrian & Marusic 2012).

Experimental evidence of hairpins in turbulent boundary layers was observed by Offen & Kline (1974, 1975), followed by Head & Bandyopadhyay (1981) who formed a structural link between the near-wall and the outer-flow behaviour. It was concluded that these structures are a major constituent of the turbulent boundary layer, and their work described several geometric properties of hairpin-like structures, including their characteristic angle to the wall and aspect ratio. One notable observation of Head & Bandyopadhyay (1981) was that hairpin vortices could organise into larger coherent groups. This important notion lead to a large range of studies investigating this phenomenon. For example, studies by Acarlar & Smith (1987*a*,*b*) showed that the insertion of a single hairpin vortex into a laminar boundary layer could generate a series of small hairpins, which then travel as a group (packet) with a common convection velocity. The notion of coherent packets of hairpins evolving from independent hairpin structures was also demonstrated in simulations by Zhou *et al.* (1999).

Alternative explanations to the hairpin-packet paradigm include the notion of 'superbursts' (Na, Hanratty & Liu 2001), where large-Reynolds-stress-producing events are observed as regions of relatively low-momentum fluid. del Álamo *et al.* (2004) showed similar structures, but attributed these log-region phenomena to passive wakes formed downstream of vortex clusters. An extension of this work by del Álamo *et al.* (2006) showed that the length and width of these clustered vortices are proportional to their wall-normal height, and further developments are reviewed by Jiménez (2012). More recently, simulations by Schlatter *et al.* (2014) at moderate Reynolds numbers have also highlighted that hairpin-like structures which extend to the wall are not observed instantaneously, in contrast to the findings of Wu & Moin (2009) (see also discussion in Marusic (2009) regarding this on-going debate). For an extensive overview of structures and coherent motions in wall turbulence, readers are directed towards recent summaries by Marusic & Adrian (2012) and Herpin *et al.* (2013), and more recent developments concerning large- and very-large-scale motions are discussed in Baltzer, Adrian & Wu (2013) and Lee *et al.* (2014).

Meinhart & Adrian (1995) reported the existence of large and irregularly shaped regions of uniform streamwise momentum (hereafter referred to as a uniform momentum zone, or UMZ). They reported that these UMZs were commonly observed encapsulating the logarithmic region. Meanwhile, the wake region of the boundary layer seemed to be populated with complicated and time-varying patterns of zones of uniform streamwise momentum. This zonal structural arrangement is best described with reference to figure 1(*a*), where a randomly selected streamwise–wall-normal velocity field is shown from a particle image velocimetry (PIV) measurement to be described shortly. Qualitatively, the zonal-like structure in the streamwise velocity is evident by visual inspection, where three regions of relatively uniform
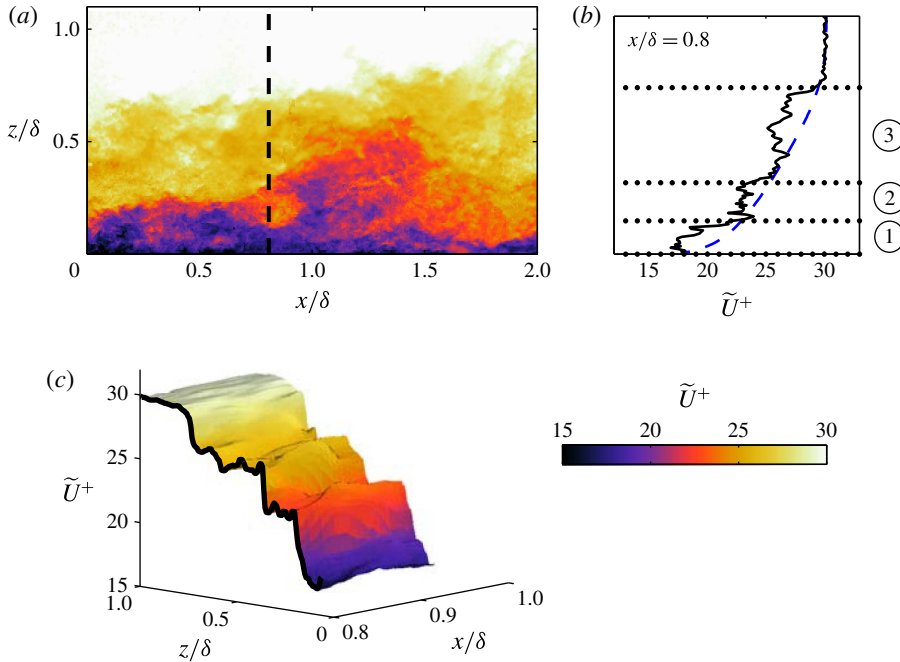
FIGURE 1. (Colour online) (*a*) Colour contours of streamwise velocity ($\widetilde{U}^+$) at $Re_\tau \approx 8000$ from a single PIV frame. (*b*) Comparison between an instantaneous (——) and mean (– –) velocity profile. Horizontal dotted lines correspond to possible separations of zones of constant streamwise momentum; for this example, three possible UMZs are observed, labelled ①, ② and ③. (*c*) Three-dimensional streamwise velocity contours for $0.85 < x/\delta < 1$ and $0 < z/\delta < 1$. The black contour line shows the instantaneous streamwise velocity profile in z at $x/\delta = 0.8$ (as also plotted in *b*).

streamwise momentum are observed for the selected velocity field at the highlighted streamwise location ($x/\delta = 0.8$, where δ corresponds to the boundary layer thickness). Closer inspection of the instantaneous mean velocity profile at $x/\delta = 0.8$ (figure 1*b*) shows that, unlike the average velocity profile (shown by the blue dashed line), the instantaneous counterpart consists of sudden step-like jumps in streamwise momentum as one passes from one UMZ to another (see also figure 1*c* which shows a three-dimensional surface of the streamwise velocity ($\widetilde{U}$) in the range $0.8 < x/\delta < 1$).

A more extensive study on UMZs was detailed in Adrian *et al.* (2000), where it was shown that UMZs are prevalent and persistent for large streamwise lengths (of the order of δ). They hypothesised that these features were linked to the existence of packet-like hairpin structures, and coupled their results with numerical work from Zhou *et al.* (1999) to construct a conceptual model. This model has been shown to explain several quantitative results seen in both experimental and numerical work to date. Tomkins & Adrian (2003) performed a complementary set of experiments in the same turbulent boundary layer as Adrian *et al.* (2000) but in a streamwise–spanwise plane from the buffer layer to the top of the logarithmic region. Here, the dominant motions were shown to be large-scale, low-momentum zones elongated in the streamwise direction, which are bordered by organised vortices. Similar experimental observations were also made by Ganapathisubramani, Longmire & Marusic (2003) and Hambleton, Hutchins & Marusic (2006). Recent large-scale

direct numerical simulations (DNS) by Lee & Sung (2011) showed groups of hairpin vortices which are coherently arranged in the streamwise direction. They observed that these structures combined to create significantly elongated low- and high-momentum regions (large-scale motions) of the order of 3δ–4δ.

The presence of structural features is not easily observable with single-point measurements. However, a co-spectral analysis between the wall-normal velocity and spanwise vorticity by Priyadarshana *et al.* (2007) (later extended by Morrill-Winter & Klewicki 2013) from well-resolved hot-wire measurements showed both high- and low-wavenumber peaks. They hypothesised that the high-wavenumber peak is associated with concentrated patches of vorticity (referred to as vorticity fissures), whereas the low-wavenumber peak could be the signature of the persistent presence of UMZs. They related the vorticity fissures to the step-like jumps in the instantaneous streamwise velocity as one moves away from the wall (see figure 1*b*). These results support the zonal-like structural arrangement in turbulent boundary layers.

The importance of hairpin structures (at least as a statistical construct) was also demonstrated in the models of Perry and co-workers (see Perry & Chong 1982; Perry, Henbest & Chong 1986; Marusic & Perry 1995; Perry & Marusic 1995) in which the boundary layer is conceived as a collection of randomly located attached eddies. These models were the first to use a hairpin vortex shape as the representative eddy in a kinematic model for wall turbulence, and are based on Townsend's attached eddy hypothesis (Townsend 1976). These studies showed that the inclusion of certain eddy geometries representative of hairpin-like structures in the model enabled the accurate reproduction of flow statistics, including the Reynolds stresses and, more recently, structure functions (de Silva *et al.* 2015; Woodcock & Marusic 2015). Marusic (2001) incorporated coherence between the individual hairpin-shaped eddies to form packets (trains of eddies) into the model to align with experimental observations. Results showed improved agreement between the model and experimental statistics for velocity correlations and structure angles based on two-point correlations. This suggested that spatially coherent packets are a statistically significant structure in the logarithmic region of turbulent boundary layers.

A decade and a half after the work of Adrian *et al.* (2000), the present study aims to analyse the structural framework associated with UMZs in turbulent boundary layers using databases that span over a decade of Reynolds numbers. This enables us to significantly extend the range of scales used in previous work to unambiguously observe any characteristic properties of UMZs as a function of Reynolds number. First, we aim to carefully examine the criterion used to detect UMZs described in Adrian *et al.* (2000). Thereafter, this criterion is applied to both experimental and simulation databases to reveal a clear log-linear increase in the number of UMZs with increasing Reynolds number. Furthermore, we explore the predictive capability of synthetic velocity fields generated using the attached eddy model, in reproducing a similar zonal-like structural arrangement and Reynolds number dependence.

The paper is organised as follows: § 2 provides a description of the experimental databases used. Section 3 examines the detection criterion employed, together with some associated caveats which are described further in appendix A. The main results obtained from each dataset are presented in § 4 and are complemented by findings described in § 5 from the attached eddy model. Finally, § 6 describes further statistical properties of UMZs.

Throughout this paper, the coordinate system *x*, *y* and *z* refers to the streamwise, spanwise and wall-normal directions, respectively. Corresponding instantaneous streamwise, spanwise and wall-normal velocities are represented by $\widetilde{U}$, $\widetilde{V}$ and $\widetilde{W}$,

Experiment	Re_τ	U_∞ (m s^{-1})	U_τ (m s^{-1})	δ (m)	$L_x \times L_z$	Δx^+, Δz^+	Overlap (%)	PIV frames
Hambleton *et al.* (2006)	1 200	6	0.25	0.07	$1.5\delta \times 1.3\delta$	32×32	50	1478
Adrian *et al.* (2000)	2 800	11.4	0.41	0.10	$1.4\delta \times 1.3\delta$	36×26	50	50
de Silva *et al.* (2014a)	7 900	10	0.33	0.36	$2\delta \times 1.1\delta$	40×40	50	1000
de Silva *et al.* (2014a)	14 500	20	0.63	0.35	$2\delta \times 1.1\delta$	40×40	50	1000

TABLE 1. Experimental parameters of the four PIV databases employed. $L_x \times L_z$ corresponds to the field-of-view (FOV) of the streamwise–wall-normal plane, and Δx^+ and Δz^+ correspond to the interrogation window size: it equals $\Delta x^+ \times \Delta z^+$ for the datasets from Adrian *et al.* (2000) and Hambleton *et al.* (2006) at all wall locations; for de Silva *et al.* (2014a), it equals $\Delta x^+ \times \Delta z^+$ and $1.6\Delta x^+ \times 1.6\Delta z^+$ for the ranges $z/\delta < 0.4$ and $z/\delta > 0.4$, respectively; however, the vector grid spacing is matched across the entire extent of the dataset.

respectively, with the corresponding velocity fluctuations given by lower-case letters. Overbars indicate averaged quantities, and the superscript + refers to normalisation by inner scales. For example, we use $l^+ = lU_\tau/\nu$ for length and $\widetilde{U}^+ = \widetilde{U}/U_\tau$ for velocity, where U_τ is the friction velocity and ν is the kinematic viscosity of the fluid.

2. Experimental databases

The present study utilises data from several planar PIV experiments, all acquired on a streamwise–wall-normal plane. The selected databases span over a decade in Reynolds numbers, $Re_\tau \approx 1200$–14 500. Key experimental parameters of each database are summarised in table 1. Further details on each dataset can be found in their respective publications (also listed in table 1). It should be noted that for consistency δ and U_τ are recomputed by applying the composite velocity profile of Chauhan, Monkewitz & Nagib (2009). This yields a boundary layer thickness that is approximately 18 % greater than δ_{99}.

The following analysis requires PIV datasets with adequate spatial resolution and dynamic spatial range, simultaneously. Achieving this is challenging at high Reynolds numbers, where the range of scales of turbulent motion becomes large. The high Reynolds number datasets employed in the present study are acquired with this goal in mind, using a unique experimental setup with multiple cameras to obtain a large field-of-view (streamwise extent $>2\delta$), with targeted spatial resolution where it is most critical (closer to the wall). Further details on the accuracy of the data and the influence of spatial resolution can be found in de Silva *et al.* (2014a). We note that some degree of spatial filtering is to be expected from PIV datasets; however, we anticipate that the structural features analysed in this study will not be affected adversely by this limitation. In any case, the viscous-scaled interrogation window size for all four datasets used here are rather similar, and as such they should experience nominally comparable spatial attenuation.

3. Detection of zones of uniform momentum

By definition, a UMZ must encapsulate a region of fluid with roughly uniform streamwise velocity magnitude. This leads to local maxima in the probability density
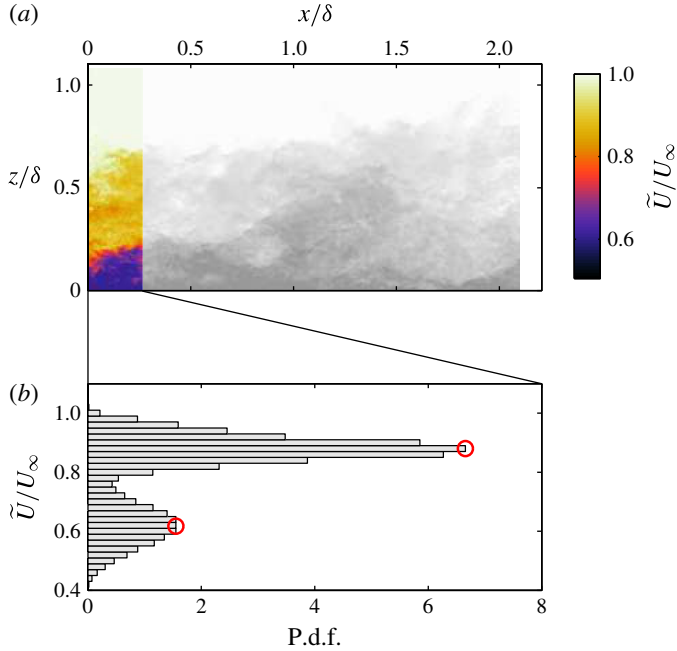
FIGURE 2. (Colour online) Illustration of detection criterion for UMZs applied to an instantaneous velocity field at $Re_\tau = 8000$. (*a*) Iso-contours of streamwise velocity ($\widetilde{U}$) of the included region of a single PIV frame (colour, $0 \lesssim x/\delta \lesssim 0.25$), and omitted region in gray-scale. The colourbar for the included region is shown on the right. (*b*) The histogram of $\widetilde{U}/U_\infty$ constructed using the included region indicated in (*a*); ○ symbols indicate the detected modal velocities. The non-turbulent region is not included in constructing the p.d.f. shown in (*b*).

histograms (p.d.f.) of the streamwise velocity component (Adrian *et al.* 2000). These local maxima are expected to be associated with the streamwise momentum of each zone, and the corresponding velocity magnitude is referred to as a modal velocity. The detection criterion employed is illustrated in figure 2, where figure 2(*a*) shows a sample velocity field spanning 2δ obtained at $Re_\tau \approx 8000$ with the included region shown using colour contours on the left (i.e. $0 \lesssim x/\delta \lesssim 0.25$ or up to 2000 viscous units). The corresponding histogram of the streamwise velocity in the included region is shown in figure 2(*b*), where the peaks of this p.d.f. correspond to possible modal velocities ($\widetilde{U}_m$, indicated by ○ symbols). The example shows two clear peaks in the p.d.f. (modal velocities) whose corresponding UMZs are also identifiable by visually inspecting figure 2(*a*).

It should be noted that the non-turbulent region where $\widetilde{U} \approx U_\infty$ is not included in the p.d.f. of figure 2(*b*) by omitting all velocity vectors beyond the turbulent/non-turbulent interface (TNTI). The location of the TNTI is detected by employing a threshold on the kinetic energy defect (or defect in kinetic energy) of the flow (with a frame of reference moving with the free stream). Such a technique has been shown previously to work well with similar PIV data (see de Silva *et al.* 2013; Chauhan *et al.* 2014; Philip *et al.* 2014). Following Chauhan *et al.* (2014), the appropriate threshold is chosen by matching the intermittency profile for each dataset to other datasets (hot-wire) using an error function. This omission of velocity vectors is necessary as

the strong modal velocity caused by the uniform non-turbulent region inhibits the detection of other modal velocities in the vicinity of the free-stream velocity. Further, for consistency, only the region above $z^+ > 100$ is included for all datasets as the velocity fields in the near-wall region are not captured by the PIV (especially for the high-Re_τ datasets).

Many investigators have measured the p.d.f. of velocities in wall-bounded flows. However, the measurements typically involved time-averaging the p.d.f. over a long period and/or averaging at only a single wall-normal location. Any of these operations will smooth out the detection of UMZs as noted by Adrian *et al.* (2000). The streamwise length of the PIV velocity field ($\mathscr{L}_x$) from which the p.d.f. is constructed also plays an important role. A field of view (FOV) with insufficient streamwise length for this study may lead to an insufficient number of velocity vectors (or grid points) for convergence. Meanwhile, if $\mathscr{L}_x$ is much larger than the streamwise extent of the UMZs, the local maxima (modal velocities) would tend to be smoothed out since $\mathscr{L}_x$ introduces an implicit filter on the p.d.f. We note however that a careful examination of the influence of $\mathscr{L}_x$ (and other parameters) on the number of detections shows minimal impact (see appendix A for further details). To summarise, the range utilised previously by Adrian *et al.* (2000), where $\mathscr{L}_x \approx \delta$ (or approximately 2000 viscous units) is shown to be a reasonable choice, and therefore we will employ the same range for the subsequent analysis. However, our results show that $\mathscr{L}_x$ should be chosen based on viscous units rather than outer scaling (δ), as previously prescribed by Adrian *et al.* (2000).

To elaborate further, if $\mathscr{L}_x$ is scaled on outer units (δ) for the high-Re datasets, L_x would be $O(Re_\tau)$, which would inhibit our ability to determine the modal velocities of UMZs associated with the smallest coherent motions (which is a viscous-dependent lower bound). Conversely, the modal velocities of larger UMZs that exceed $\mathscr{L}_x$ are readily detectable due to their large spatial signature on the velocity field. Therefore, we conclude that $\mathscr{L}_x$ should be chosen to be sufficiently small and scaled in viscous units to determine the modal velocities of the smaller UMZs (which also scale in viscous units). We note that for the lowest Re_τ dataset of Hambleton *et al.* (2006), which does not have a streamwise FOV exceeding 2000 viscous units, we used the full streamwise extent of each instantaneous velocity field of approximately 1600 viscous units. Other important considerations include the number of bins used to form the p.d.f. and the number of velocity vectors (or grid points) available to construct the p.d.f. For consistency, both quantities are fixed for all datasets, with 50 bins and $\approx 5 \times 10^3$ velocity vectors used to construct each p.d.f. at $\mathscr{L}_x^+ \approx 2000$. A change in the number of velocity vectors by halving or doubling is found to have negligible effect on the computed numerical values (see appendix A) and the general conclusions are insensitive to an even bigger change.

There is a possibility that UMZs with small spatial extents may go undetected due to the $\mathscr{L}_x$ required to obtain sufficient ensembles to construct the p.d.f. As a consequence, we expect that an increase in spatial resolution may enable us to use a smaller $\mathscr{L}_x$, while still maintaining sufficient velocity vectors to construct the p.d.f. Nevertheless, we again do not expect the conclusions drawn in this study to be sensitive to this, as will be shown quantitatively in §4 by using a well-resolved DNS dataset at moderate Re_τ.

It is worth highlighting that a similar detection criterion was employed recently to study the uniform momentum core in turbulent channel flows, where it was shown that this region was successfully demarcated by considering the p.d.f.s of the streamwise velocity component (Kwon *et al.* 2014). As a final note, when considering this type
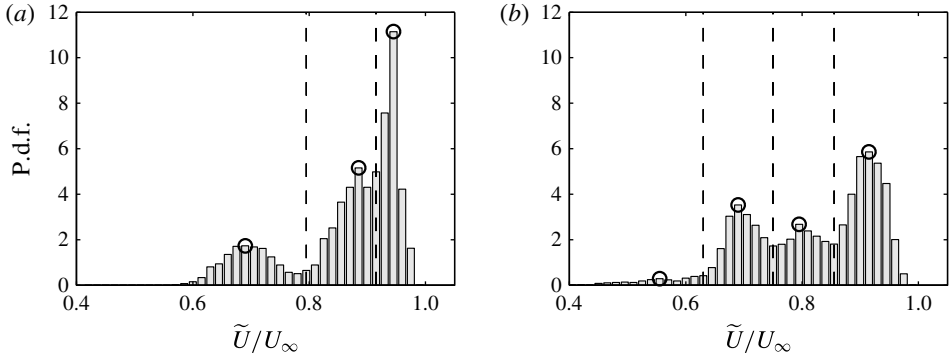
FIGURE 3. P.d.f. of the instantaneous streamwise velocity ($\widetilde{U}$) normalised by U_∞ at (*a*) $Re_\tau \approx 8000$ and (*b*) $Re_\tau \approx 14\,500$. Each p.d.f. corresponds to a randomly chosen PIV frame with ○ corresponding to the detected modal velocities. The vertical dashed lines show the edges of these UMZs (mid-point of the detected modal velocities).

of analysis using p.d.f.s of velocity from PIV datasets, any pixel-locking (pixel displacements which are biased to integers, see Adrian & Westerweel 2011) should be carefully dealt with. A careful examination of the influence of peak locking on the detection of UMZs and how it is minimised is provided in de Silva, Hutchins & Marusic (2014*b*). To summarise, the bias in the velocity field to integer displacements also affects the magnitude of the detected modal velocities in a similar fashion. A comparable influence of pixel-locking on modal velocities was also shown in a PIV dataset from a turbulent channel flow by Kwon *et al.* (2014). For the present analysis the degree of pixel-locking for all datasets has been checked and found to be minimal (quantified further in de Silva *et al.* 2014*b*).

4. Characterisation of uniform momentum zones

In this section, we analyse the experimental databases using the detection criterion described in § 3 to explore the structural characteristics of UMZs. Figures 3(*a*) and 3(*b*) show p.d.f.s of the streamwise velocity component from randomly chosen PIV images at $Re_\tau \approx 8000$ and $Re_\tau \approx 14\,500$, respectively with $\mathscr{L}_x^+ \approx 2000$. The detected modal velocities of each UMZ are indicated by the ○ symbols, and the vertical dashed lines correspond to the streamwise velocity magnitude that separates neighbouring UMZs. For the present study, the magnitude of the streamwise velocity that demarcates each detected UMZ is approximated by the mid-point between modal velocities of neighbouring UMZs and the location of the TNTI. The corresponding instantaneous streamwise velocity field for each p.d.f. from figure 3 is shown in figure 4(*a,c*). The edges of each detected UMZ are represented by the solid lines, which are overlaid on colour contours of streamwise velocity. Qualitatively, it is evident that the detected edges of UMZs are accompanied by a sudden change in the streamwise velocity in the wall-normal direction (high $\partial\widetilde{U}/\partial z$). We observed similar characteristics in other PIV frames from all four PIV databases, thus providing a certain degree of validity to the approach used to detect the edges of UMZs. Also noted is the presence of patches of high $\partial\widetilde{U}/\partial z$ along each boundary/edge (see figure 4*b,d*), which show colour contours of $\partial\widetilde{U}/\partial z$). Previously, Meinhart & Adrian (1995), Adrian *et al.* (2000) and others postulated that these patches of
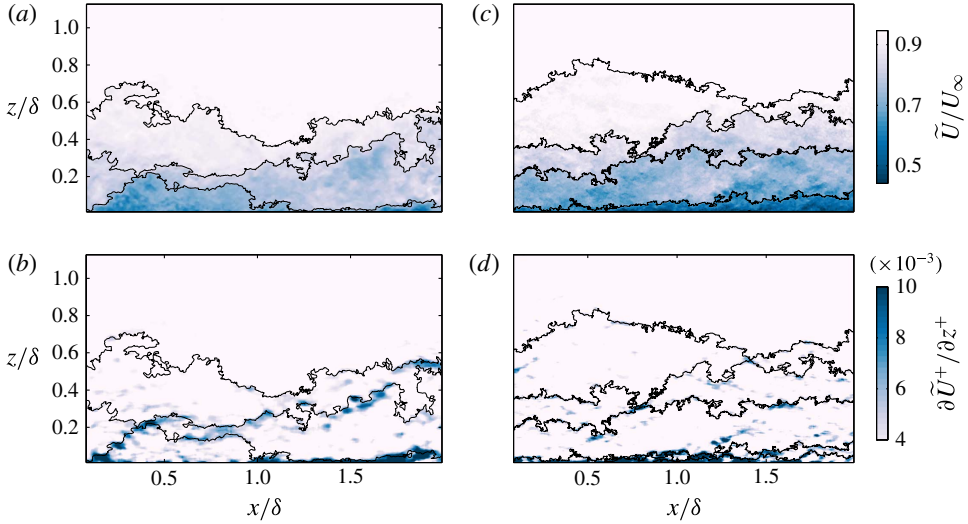
FIGURE 4. (Colour online) Edges of UMZ determined using modal velocities and location of TNTI: (*a*,*c*) overlaid on colour contours of streamwise velocity ($\widetilde{U}$) from a single PIV frame at $Re_\tau \approx 8000$ and $Re_\tau = 14\,500$, respectively; (*b*,*d*) overlaid on $\partial\widetilde{U}/\partial z$ at $Re_\tau \approx 8000$ and $Re_\tau = 14\,500$, respectively.

high $\partial\widetilde{U}/\partial z$ mark the possible presence of packet-like structures or vortex fissures (see Klewicki 2010), where a significant proportion of the spanwise vorticity is concentrated (Priyadarshana *et al.* 2007). Although an interesting topic, any attempts to correlate the UMZ with vortical structure would ideally require both temporally and spatially resolved datasets. In this case the available data are more suited to an analysis of the distribution of UMZs as a function of Reynolds number.

Figure 5(*a*) shows p.d.f.s of the number of UMZs (N_{UMZ}) detected at various Reynolds numbers from the experimental databases. The results reveal a clear increase in N_{UMZ} with increasing Reynolds number. Adrian *et al.* (2000) hypothesised that the observed UMZs are caused by the presence of highly organised hairpin-like structures that form packets. If one agrees with this hypothesis, we may observe an increase in N_{UMZ} with increasing Reynolds number as the range of scales increases. Previously, no quantitative evidence of this variation in N_{UMZ} was observed; however, this may be caused by the limited range and magnitude of Reynolds numbers considered. The present study considers a range of Reynolds numbers that span over a decade (with sufficient scale separation), enabling us to better discern if such a trend exists.

Figure 5(*b*) shows the mean N_{UMZ} ($\overline{N}_{UMZ}$) across the range of Reynolds numbers studied. The results indicate that $\overline{N}_{UMZ}$ has a logarithmic increase with Reynolds number (indicated by the dashed line). As will be seen in § 5, this provides strong evidence of a hierarchical length-scale distribution of structures within the boundary layer. To complement the experimental databases the $\bigcirc$ symbols correspond to the same analysis applied to a recent DNS database at two Reynolds numbers $Re_\tau \approx 1600$ and $Re_\tau \approx 2500$ (Sillero *et al.* 2013). For the present study, 100 independent streamwise–wall-normal (*xz*) planar velocity fields are extracted from the DNS databases for both Reynolds numbers. The parameters of these velocity fields are matched to the experimental database at a comparable *Re*, these include: spatial domain size, resolution and velocity vector grid spacing. Furthermore, we
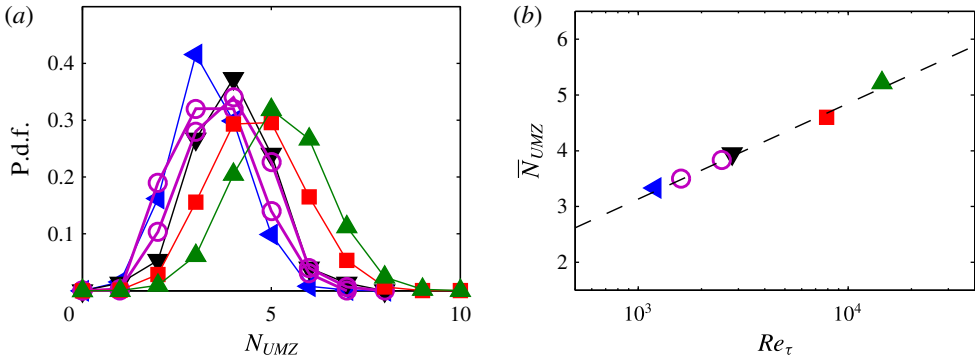
FIGURE 5. (Colour online) (*a*) P.d.f. of the number of UMZs detected at varying Reynolds numbers from the experimental databases: ◄, ▼, ■, ▲ symbols correspond to datasets at $Re_\tau \approx 1200$, $Re_\tau \approx 2800$, $Re_\tau \approx 8000$, $Re_\tau \approx 14\,500$, respectively. (*b*) Mean number of UMZs ($\overline{N}_{UMZ}$) at varying Reynolds numbers detected from the experimental databases. The ○ symbols corresponds to a recent DNS database at $Re_\tau \approx 1600$ and 2500 (Sillero, Jiménez & Moser 2013).

only consider the region above $z^+ > 100$, thereby matching the available region in the experimental datasets. Our analysis shows that a variation in spatial filtering and grid spacing of the DNS datasets has negligible influence on the results presented; however, for consistency it is important to omit the near-wall region ($z^+ < 100$) which is unavailable in the experimental datasets. It is also worth highlighting that since these parameters are matched between the simulation and experimental databases, the p.d.f. of streamwise velocity and subsequently the performance of the detection criterion for UMZs are comparable, and are therefore not reproduced here for brevity. The results in figure 5 for the number of UMZs show good agreement between the DNS and experimental databases at a comparable Reynolds number, which further emphasises the robustness of the *Re* trends observed with the experimental databases over a larger range. It should be noted that while some uncertainty remains about using modal velocities to detect UMZs and their associated boundaries, the trends with Reynolds number are robust. Additionally, based on our results, we have observed robust and qualitatively sensible detections in all PIV databases considered, which has been aided by the utility of the automated processing procedure.

The analysis to follow will employ the models described in the work of Perry and co-workers (Perry & Chong 1982, and others) which describe the boundary layer statistics using a collection of randomly located attached eddies with a hierarchical length-scale distribution. This model provides further insight into the zonal-like structure in turbulent boundary layers observed from experimental work.

5. Revisiting the attached eddy model

The attached eddy model has been shown to reproduce flow statistics of wall-bounded turbulence reasonably well (Marusic & Perry 1995; Perry & Marusic 1995). Here, we use the model to go beyond statistics and employ it to generate synthetic instantaneous velocity fields. The synthetic velocity fields (hereafter referred to as attached eddy model (AEM) velocity fields) are generated using a structural arrangement similar to that described in Marusic (2001), with hierarchies of eddies randomly distributed in groups or packets of hairpin vortices (hereafter referred
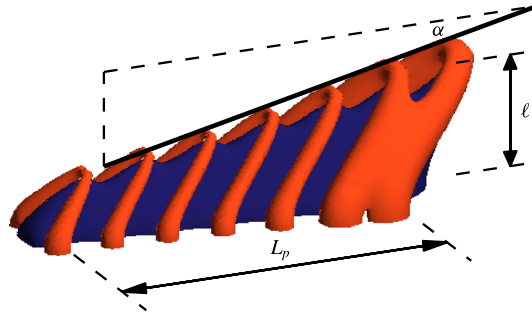
FIGURE 6. (Colour online) Schematic of a typical representative Λ packet-eddy. The blue region isolates the low-momentum UMZ formed beneath the train of Λ-eddies corresponding to $\Delta U^+_{eddy} < -0.3$; the red region corresponds to a higher speed ($\Delta U^+_{eddy} > 0.05$). Here α is the inclination angle of the packet and ℓ is the wall-normal height of the largest eddy in the packet. L_p represents the streamwise extent of the packet based on the spacing of eddies within it.

to as packet-eddies). The AEM is then utilised to extract streamwise–wall-normal planes with a spatial domain and resolution equivalent to the experimental datasets investigated previously. Over 500 such planes are extracted, enabling us to calculate well-converged statistics. A brief description of the model, with emphasis placed on the generation of the synthetic velocity fields, is presented next (full details of the model can be found in Marusic & Perry 1995, Perry & Marusic 1995). For the present analysis, in addition to investigating UMZs, the AEM synthetic velocity fields prove to be a useful utility to assess the detection criterion used thus far.

5.1. *Computing synthetic velocity fields from the AEM*

Each synthetic flow field is assumed to contain a hierarchy of packets generated from Λ-eddies such as the example shown in figure 6. For the present study each representative packet-eddy consists of seven Λ-eddies with an average eddy spacing of 0.4ℓ (where ℓ is the wall-normal height of the largest eddy in the packet) and an inclination angle $\alpha = 10°$, which are chosen based on prior work by Marusic (2001). First, the velocity field for a single representative Λ-eddy is computed using the Biot–Savart integral, where a Gaussian distribution of vorticity is assumed in the cores of the vortices or rods that constitute each Λ-eddy (Perry & Marusic 1995). Thereafter, the superposition of the velocity fields from each Λ-eddy within a packet (together with their image eddies in the wall) provides a representative flow field consisting of a single packet scale. This process is then repeated at different hierarchical length scales to obtain the complete AEM velocity field. The representative length scales follow a geometric progression from one hierarchy to another with self-similarity between flow fields from different hierarchies. We note that this self-similarity can be exploited to minimise the computation cost of generating AEM velocity fields, as the Biot–Savart calculations are only computed once. It should be noted that the placement of each packet-eddy in the plane of the wall is perfectly random, whereas the height of each packet-eddy follows a probability density function that adheres to the geometric progression stated in Perry *et al.* (1986). These distributions ensure that a log law is returned for the mean flow and $\overline{u^2}$ statistics.

Previously, Marusic (2001) established that the inclusion of representative eddies in a packet-like structure explained the velocity correlation trends observed in a turbulent

Symbol	Re_τ	Eddy hierarchies	$L_x \times L_z$	$\Delta x^+,\ \Delta z^+$	Frames
■	800	4	$2\delta \times 1.2\delta$	30×30	500
▲	1 600	5	$2\delta \times 1.2\delta$	30×30	500
◄	3 200	6	$2\delta \times 1.2\delta$	30×30	500
►	6 400	7	$2\delta \times 1.2\delta$	30×30	500
●	12 800	8	$2\delta \times 1.2\delta$	30×30	500

TABLE 2. Parameters of the attached eddy model (AEM) synthetic datasets. The number of eddy hierarchies corresponds to different energetic scales present in the AEM velocity fields at a particular Re_τ. Other parameters are defined in table 1.

boundary layer, particularly within the logarithmic region. Although not pursued by Marusic (2001) it was highlighted that the reproduction of quantitatively accurate mean flow and Reynolds stresses in the turbulent boundary layer would require refinement to the shape parameters associated with the representative packet-like eddy structure. Since this study primarily focuses on UMZs in turbulent boundary layers, we will not attempt to precisely match all the Reynolds stress components for the generated synthetic velocity fields (shown previously for a non-packet-like structure, using multiple eddy shapes by Marusic & Perry 1995, Perry & Marusic 1995). Furthermore, we have not attempted to modify the model (or pursued improvements to the model) to match the experimental results; rather, we employ it as a tool to provide insight into the representative structures that are likely to be responsible for the zonal-like structure observed experimentally. However, emphasis is placed on accurately replicating the velocity deficit across the boundary layer in order to attain a comparable distribution of streamwise momentum in the AEM velocity fields similar to the experimental databases. Further details on computing the appropriate scaling and population density of the eddies for the synthetic velocity fields to attain an accurate description of the velocity deficit are provided in appendix B. To summarise, the synthetic velocity fields are scaled such that $\overline{uw}^+|_{peak} \approx 1$ in the log region, which has been empirically observed at sufficiently high Reynolds numbers. Further, the spatial population density of the eddies is chosen such that we obtain the log-law constants to match the experimental results (with $\kappa \approx 0.39$ and $A \approx 4.3$).

For this study, synthetic velocity fields are generated spanning a large proportion of the *Re* range studied experimentally from $Re_\tau = 800$ to $Re_\tau = 12\,800$. Table 2 summarises key parameters of the AEM velocity fields. Reynolds numbers below $Re_\tau = 800$ are omitted as the boundary layer is not typically considered to be fully turbulent (Klewicki, Ebner & Wu 2011). Other parameters such as the FOV and spatial resolution are closely matched to the experimental databases summarised in table 1. Following Perry and co-workers, we fix the smallest packet-eddy length scale to be on the order of $100\nu/U_\tau$ (following the Kline *et al.* 1967 scaling), after which the number of hierarchical packet-eddies (N_h) follow a geometric progression with Reynolds number.

A few representative packet-eddy shapes are considered for this analysis, including Λ-eddies, Π-eddies and slanted-Π eddies. Figures 7(*a*) and 7(*b*) show a qualitative comparison between an experimental velocity field at $Re_\tau \approx 8000$ and a synthetic velocity field of packets of Λ-eddies at $Re_\tau = 6400$, respectively. Visual comparison between these two instantaneous velocity fields shows a reasonable degree of similarity. One notable difference is the lack of small-scale activity away from
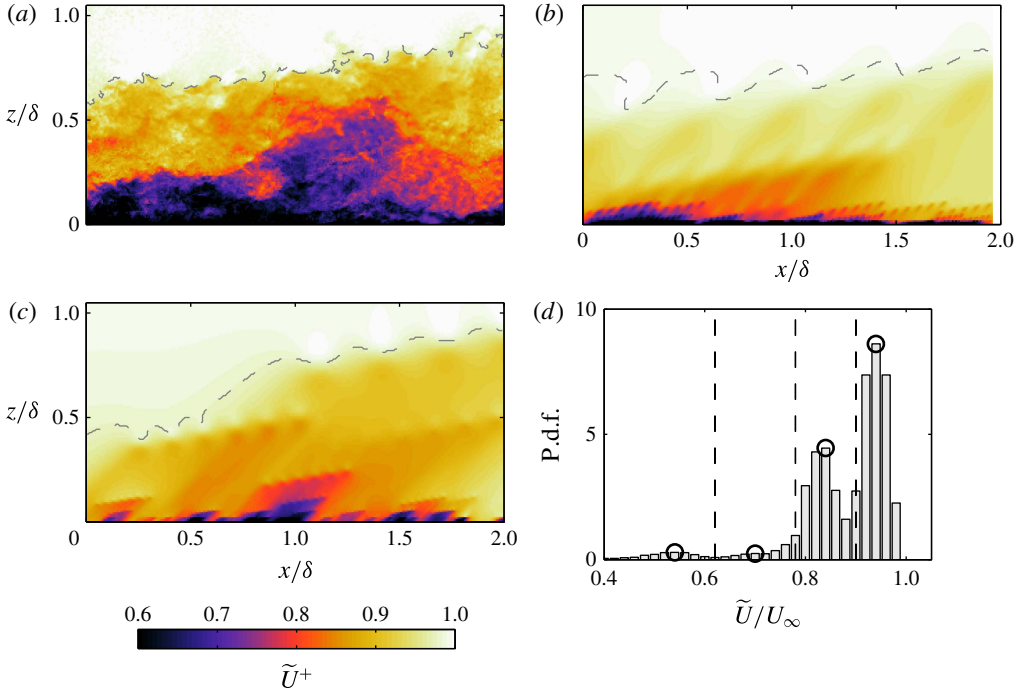
FIGURE 7. (Colour online) Colour contours of streamwise velocity ($\widetilde{U}^+$) at (*a*) $Re_\tau \approx 8000$ from a single PIV frame, (*b*) $Re_\tau = 6400$ from a synthetic velocity field generated using Λ packet-eddies, and (*c*) as (*b*) but using Π packet-eddies. The dashed line corresponds to the TNTI. (*d*) Figure 3 (p.d.f. of streamwise velocity, $\widetilde{U}/U_\infty$) reproduced using the AEM velocity field shown in (*b*).

the wall for the AEM velocity fields. However, qualitative evidence of a zonal-like structural organisation within the turbulent boundary layer is easily observable, and consistent in all synthetic velocity fields generated. An examination of the p.d.f. of $\widetilde{U}$ (see example in figure 7*d*) from the AEM synthetic velocity also shows similar evidence indicating the presence of UMZs. Figure 7(*c*) shows a synthetic velocity field generated using Π-eddies. Although not reproduced here, the statistical behaviour of both representative packet-eddy shapes is quite similar, and therefore the subsequent analysis employs Λ-eddies due to their qualitatively accurate representation of a turbulent boundary layer and geometric simplicity. Furthermore, in spite of the fact that we have considered hairpin-like structures as the representative eddy for our synthetic velocity fields, this is by no means a unique solution. In fact, we anticipate a large variety of representative eddy shapes to show both the presence of and also yield a comparable distribution of UMZs, provided the size of the energetic scales increases with distance from the wall as described in the model.

5.2. *UMZs and attached eddy model*

Here we use the UMZ detection algorithm described earlier for the experimental results to quantify the number and distribution of uniform momentum zones from the AEM velocity fields. Figures 8(*a*) and 8(*b*) show the p.d.f. and the mean number of UMZs ($\overline{N}_{UMZ}$), respectively, from the AEM datasets. It should be noted that a
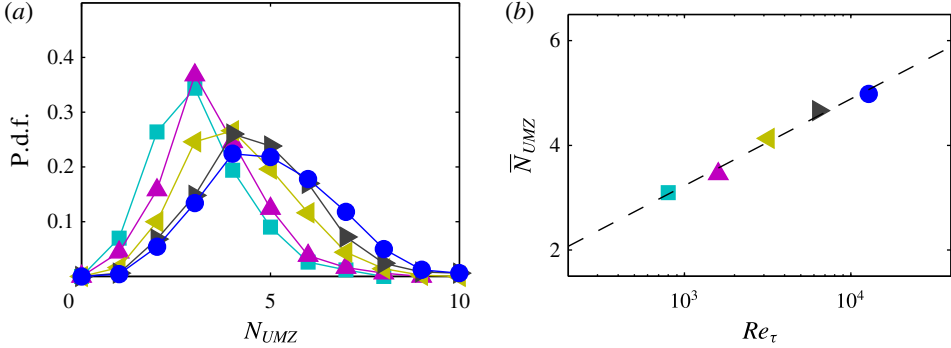
FIGURE 8. (Colour online) (*a*) P.d.f. of the number of UMZs detected in the AEM velocity fields with $\mathscr{L}_x^+ = 2000$ at varying Reynolds numbers. Symbols are defined in table 2. (*b*) Mean number of UMZs ($\overline{N}_{UMZ}$) at varying Reynolds numbers detected in the AEM velocity fields.

fixed streamwise length of $\mathscr{L}_x \approx 2000$ is used to detect modal velocities, with the exception of the lowest *Re* dataset (where $\mathscr{L}_x \approx 1600$, due to the limited FOV). The results show that the distribution of N_{UMZ} is quantitatively comparable to that obtained experimentally in §4. Furthermore, our results show that $\overline{N}_{UMZ}$ computed from the AEM velocity fields has a logarithmic increase with Reynolds number, indicated by the dashed line on figure 8(*b*). Since the number of packet-eddy hierarchies has a log-linear increase with *Re*, these results also indicate that the detection criterion captures the larger number of hierarchies present at higher *Re*.

Figure 9 shows the average number of UMZs detected at each Reynolds number considered from both the experimental databases (coloured symbols) and the AEM synthetic datasets (★ symbols). Results show good collapse of the observed logarithmic increase in $\overline{N}_{UMZ}$ with Re_τ between the experimental and AEM synthetic datasets. Consequently, we may postulate that the associated structures responsible for generating UMZs are likely to have population densities and hierarchical length-scale distributions similar to those described in the attached eddy model. This provides some insight into the representative structures that are likely to be responsible for the generation of a zonal-like structure in turbulent boundary layers.

6. Further discussion

At each Reynolds number considered, N_{UMZ} varies for each instantaneous velocity field. One possible explanation of this variation from one instantaneous velocity field to another is the variation in the instantaneous boundary layer height (δ_i) or, equivalently, the location of the turbulent/non-turbulent interface (TNTI). To investigate this further, we consider a joint p.d.f. between N_{UMZ} and δ_i, which is shown in figure 10 for the experimental dataset at $Re_\tau \approx 8000$. The results show no discernible shift in the peak location (● symbols) at every contour line presented, indicating no preference of a particular N_{UMZ} for a certain δ_i/δ (see figure 10*b*). As a consequence, one would expect the thickness of UMZs to change with δ_i. Qualitatively this result is observable on instantaneous velocity fields such as the example shown in figure 4(*c*) (for example, at $x/\delta \approx 1.5$ where δ_i is small, UMZs are observed with a reduced thickness). Similarly, at large δ_i ($x/\delta \approx 0.5$) additional UMZs are not
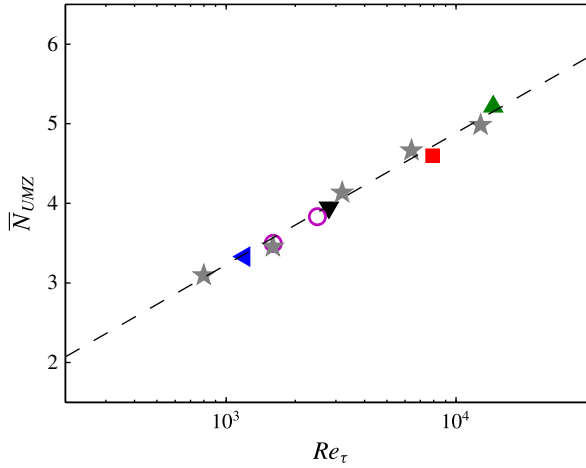
FIGURE 9. (Colour online) Comparison of the mean number of UMZs ($\overline{N}_{UMZ}$) at varying Reynolds numbers for both the experimental data (symbols are defined in figure 5) and the AEM velocity fields ($\bigstar$ symbols).
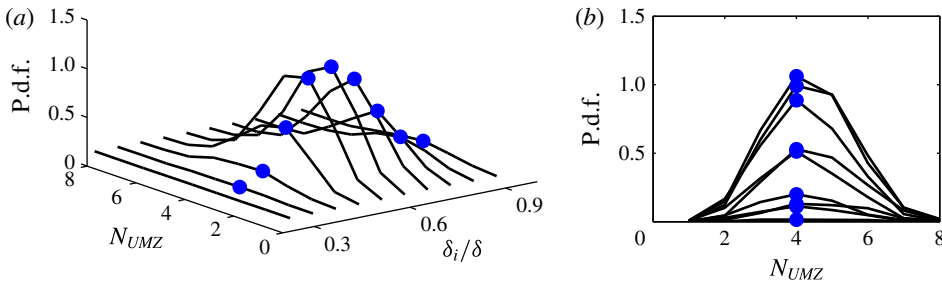

FIGURE 10. (Colour online) (*a*) Joint p.d.f. of the number of UMZ (N_{UMZ}) and the instantaneous boundary layer height (δ_i) at $Re_\tau \approx 8000$. Peaks observed in each contour are indicated by $\bullet$ symbols. (*b*) Two-dimensional projection of (*a*).

observed (instead the thickness of the UMZs seems to increase). Similar results are also observed from the other datasets, although not reproduced here for brevity.

The schematic shown in figure 11(*a*) illustrates selected geometrical properties of UMZs. The lengths z_{upper} and z_{lower} indicate the upper and lower boundaries of the UMZ encapsulated by the red contour lines, and t_{UMZ} corresponds to the thickness of the same UMZ (computed using $t_{UMZ} = z_{upper} - z_{lower}$). Figure 11(*b*) shows a p.d.f. of t_{UMZ} for all detected UMZs. Each colour represents UMZs that are composed of modal velocities ($\widetilde{U}_m$) in a particular range of momentum deficit ($(U_\infty - \widetilde{U}_m)/U_\tau$). Here, we note that a larger momentum deficit can be considered to be closer to the wall (smaller z^+) and vice versa. The p.d.f. of t_{UMZ} at varying momentum deficit (wall-normal location) shows a positive skewness, which is expected since t_{UMZ} must always be greater than zero.

Figure 11(*c*) shows the mean thickness of UMZs ($\bar{t}_{UMZ}$) for varying momentum deficit. Results show that as the momentum deficit of the UMZs increases (i.e. approaching the wall), the normalised UMZ thickness, $\bar{t}_{UMZ}/\delta$, decreases and vice versa. This is not surprising if one subscribes to a hierarchically increasing
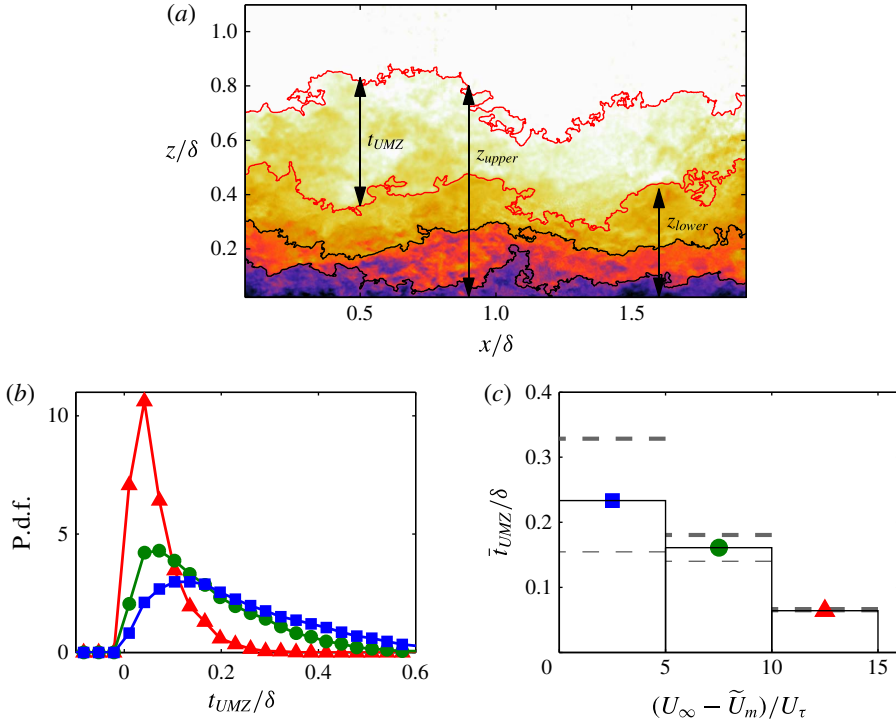
FIGURE 11. (Colour online) (*a*) Parameters describing UMZ encapsulated by the red solid lines. The lengths t_{UMZ}, z_{upper} and z_{lower} represent the thickness, upper and lower bounds of the UMZ, respectively. (*b*) P.d.f. and (*c*) mean of t_{UMZ} normalised by δ at $Re_\tau \approx 8000$. Results are binned by momentum deficit $(U_\infty - \widetilde{U}_m)/U_\tau$ with the coloured symbols corresponding to the ranges: ▲, 10–15; ●, 5–10; ■, 0–5. The horizontal thick and thin dashed lines correspond to $\bar{t}_{UMZ}$ computed including only the top and bottom 30 % of the local boundary layer thicknesses (δ_i), respectively.

length-scale distribution, where scales increase in size as they grow further from the wall (Townsend 1976; Perry & Chong 1982; Adrian *et al.* 2000). To further elucidate the influence of the local boundary thickness (δ_i) on $\bar{t}_{UMZ}$, the horizontal thick and thin dashed lines (see figure 11*c*) correspond to results computed using only the highest and lowest 30 % of δ_i wall-normal locations, respectively. The results show that an increase (or decrease) in the local boundary layer thickness (δ_i) primarily corresponds to an increases (or decrease) in thickness (t_{UMZ}) for UMZs that reside away from the wall. Conversely, UMZs closer to the wall show no significant change in t_{UMZ} as a function of δ_i. This observation can also be related to a structural arrangement, where one expects the wall-normal size of the larger hierarchies that reside in the outermost region of the boundary layer to predominantly influence δ_i, such as the models described in Townsend (1976), Perry & Chong (1982), Adrian *et al.* (2000, and others). Consequently, one would expect to associate a high δ_i with a large thickness for the UMZ furthest away from the wall and vice versa. Evidence of such a scenario is observed by examining t_{UMZ} from the AEM datasets (figure 7*b*,*c*). In this case it is clear that δ_i (shown by the dashed line) is primarily governed by the largest representative eddies (or hierarchies), with the smaller eddies closer to the wall having no discernible influence on δ_i. However, a more extensive
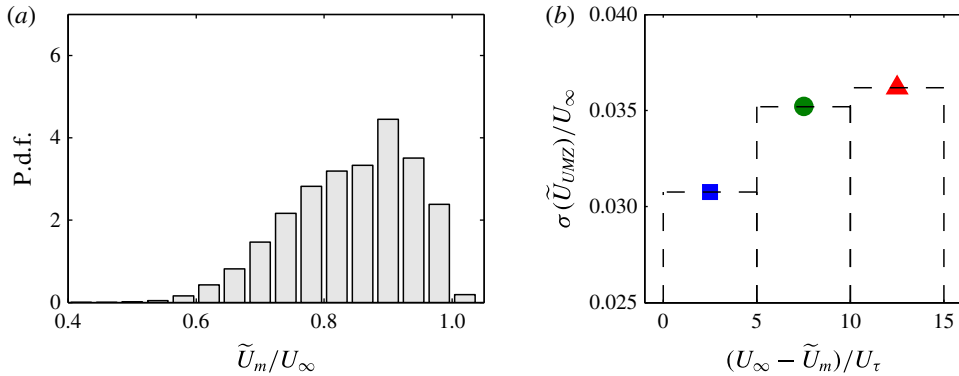
FIGURE 12. (Colour online) (*a*) P.d.f. of the modal velocities in all velocity fields at $Re_\tau \approx 8000$. (*b*) Standard deviation of the streamwise turbulent fluctuations, $\sigma(\widetilde{U}_{UMZ})$, normalised by free-stream velocity U_∞ within each detected zone relative to the local mean of $\widetilde{U}$ over the spatial region of each UMZ.

examination of t_{UMZ} inclusive of its temporal evolution would require databases that are both temporally and spatially resolved, which is unavailable in this study.

Figure 12(*a*) shows the distribution of modal velocities (here $\widetilde{U}_m$ represents the local mean of $\widetilde{U}$ over the spatial extent of each UMZ) from UMZs at $Re_\tau \approx 8000$. The results show that these regions do not have a distinctively preferred magnitude of streamwise momentum. Therefore, time averaging over a long period inhibits the observation of UMZs and their associated step-like instantaneous profiles of streamwise velocity (see figure 1); instead a smooth profile prevails. Figure 12(*b*) shows the standard deviation of the streamwise turbulent fluctuations in the UMZs ($\sigma(\widetilde{U}_{UMZ})$) binned on momentum deficit. Therefore these results provide both a quantitative measure of the streamwise turbulence intensity within each zone and its variation with wall-normal height. However, $\sigma(\widetilde{U}_{UMZ})$ should be interpreted differently to the conventional turbulence intensity since it is a measure of the variation with respect to the zonal mean. The key result here is that $\sigma(\widetilde{U}_{UMZ})$ is fairly low, providing quantitative support for the quiescence of turbulence within each UMZ. Similar turbulence levels were also reported by Kwon *et al.* (2014) within the turbulent 'core' (a UMZ observed in turbulent channel flow). It should be noted that the edges of the UMZs are not omitted from the computed statistics. Therefore, one would expect, if these regions were carefully detected and removed, the uniformity within each UMZ to be even more pronounced. In future efforts, it will be valuable to consider the three-dimensional characteristics of UMZs and also report on the causality and the temporal evolution of the zonal-like arrangement, utilising datasets that are both spatially and temporarily resolved.

7. Summary and conclusions

Through the use of a large range of experimental datasets which span over a decade of Re_τ, we investigate the structural properties of the zonal-like structure observed in turbulent boundary layers. Such an analysis is made possible by the acquisition of well-resolved high-Re_τ PIV datasets with a large field of view. The study starts with an extensive examination of a detection criterion previously suggested by

Adrian *et al.* (2000) using the probability density histograms of the streamwise velocity, followed by a confirmation of prior observations in their work. This criterion is then extended to large datasets, and is shown to be capable of isolating uniform momentum zones and their associated modal velocities.

The analysis of four experimental datasets spanning over a decade of Re_τ shows a clear log-linear increase in the number of detected UMZs with increasing Re_τ. These results reveal further evidence of an hierarchical length-scale distribution of coherent structures within the boundary layer that seem to be responsible for the observed zonal-like structure. Our findings also show an increase in wall-normal thickness of UMZs further away from the wall, which agrees with the hypothesis that length scales increase in size further away from the wall. Additionally, the average number of UMZs is unchanged when conditioned on the instantaneous boundary layer height (δ_i); instead a variation in δ_i is accompanied by a change in the wall-normal thickness of UMZs that reside furthest away from the wall. Further, results show that the detected UMZs are demarcated by regions of high $\partial \widetilde{U}/\partial z$ (shear layers/internal boundaries). These internal boundaries show a characteristic jump in streamwise velocity similar to that observed at the TNTI (Westerweel *et al.* 2005; Chauhan *et al.* 2014).

To complement the experimental databases utilised in this study, a range of synthetic datasets are generated by following the attached eddy models described in Marusic (2001), where the boundary layer is conceived as a collection of randomly located hairpin packets. The packet-like nature of the synthetic datasets are shown to generate a zonal-like organisation similar to that observed in the experimental datasets, emphasising that the model is replicating a key structural observation from recent numerical and experimental work. Analysis of the synthetic databases again reveals a log-linear increase in the number of detected UMZs with increasing Re_τ, closely matching the trend observed from the experimental results. These results suggest that in a time-averaged sense, the UMZs appear to be well-modelled by a hierarchy of self-similar structures. Furthermore, these results appear to show that the associated structures responsible for generating these UMZs are likely to have population densities and hierarchical length-scale distributions similar to those described in the attached eddy work of Perry and co-workers.

Appendix A. Detection of UMZs — important considerations

The influence of $\mathscr{L}_x^+$ is best illustrated with reference to figure 13, which shows the average number of peaks or modal velocities ($\overline{N}_{peaks}$) detected at varying $\mathscr{L}_x^+$ from the experimental datasets. Since $\mathscr{L}_x$ introduces an implicit filter on the p.d.f. we would expect to observe a decrease in the number of detections at large $\mathscr{L}_x^+$. However, in the range of $\mathscr{L}_x^+$ used for this study no significant variation in $\overline{N}_{peaks}$ is observed. Further, a clear increase in $\overline{N}_{peaks}$ with increasing Re is evident across a range of $\mathscr{L}_x^+$, showing minimal impact on the results of this study. Therefore, as previously highlighted in § 3, the range utilised previously by Adrian *et al.* (2000) where $\mathscr{L}_x^+ \approx 2000$ seems to be a reasonable choice, and so for this study we use a comparable $\mathscr{L}_x^+$ when possible. Furthermore, the range of $\mathscr{L}_x^+$ considered shows that either halving or doubling the number of ensembles available at $\mathscr{L}_x^+ \approx 2000$ (achieved by simply varying $\mathscr{L}_x^+$) has negligible effect on the computed $\overline{N}_{peaks}$.

As a final note, to ensure that the detection criterion is detecting modal velocities present in a boundary layer due to the presence of coherence in the turbulence, a counter example is utilised (shown in figure 14). This synthetic velocity field is
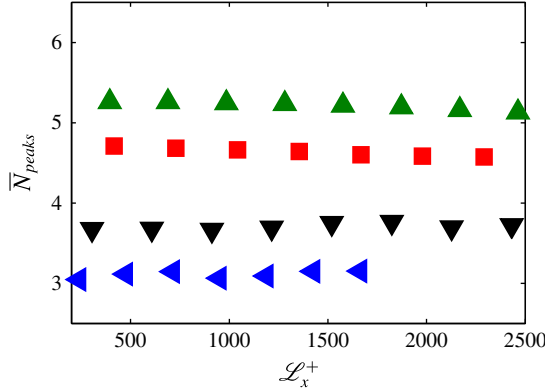
FIGURE 13. (Colour online) Influence of $\mathscr{L}_x^+$ on the number of detected peaks or modal velocities: ◄, ▼, ■, ▲ symbols correspond to datasets at $Re_\tau \approx 1200$, $Re_\tau \approx 2800$, $Re_\tau \approx 8000$, $Re_\tau \approx 14\,500$, respectively.
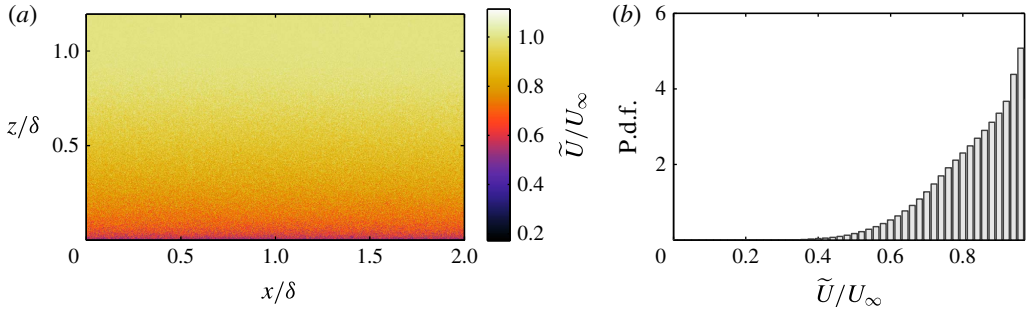

FIGURE 14. (Colour online) (*a*) Synthetic streamwise velocity field generated with mean flow and turbulence intensity equal to the dataset at $Re_\tau \approx 8000$, but with no coherence in fluctuations (Gaussian white noise). (*b*) Corresponding p.d.f. of $\widetilde{U}/U_\infty$ from velocity field (*a*), where no modal velocities are observed.

computed such that it adheres to the mean flow and turbulence intensity characteristics of a turbulent boundary layer but with the absence of any coherence in the turbulent fluctuations, thereby inhibiting the presence of UMZs (qualitatively evident in figure 14*a*). Such a scenario is established by adding Gaussian white noise to the mean flow with a magnitude representative of the turbulence intensity at each wall position. The corresponding p.d.f. of the streamwise velocity is shown in figure 14(*b*) where it is observed that no modal velocities are present (local peaks within the boundary layer) well below U_∞. As a closing note, although the Re trends described in this paper are robust, one may detect more or less modal velocities for a particular dataset based on the number of velocity vectors (or grid points), the $\mathscr{L}_x$ chosen or the proximity to the near-wall region. Therefore, when comparisons are drawn between datasets these parameters should be carefully considered.

Appendix B. Scaling of the synthetic velocity fields from attached eddy model

In this appendix, we outline how the synthetic velocity fields are scaled. However, first a brief description of the attached eddy formulation is warranted, to highlight

the parameters associated with scaling the velocity deficit and the turbulence intensity components. Following Perry & Marusic (1995) the turbulence intensity distribution can be determined by integrating over a range of length scales, ℓ, from δ_1, the smallest eddy length scale, to δ, the largest length scale (boundary layer thickness), by computing

$$\frac{\overline{u_i u_j}}{U_\tau^2} = \frac{U_0^2}{k_x k_y} \int_{\delta_1}^{\delta} \Delta(\overline{u_i u_j})\, p_H(\ell)\, d\ell, \tag{B 1}$$

where $p_H(\ell)$ corresponds to a probability distribution for each hierarchical scale $(p_H(\ell) = 1/\ell)$, U_0 is the characteristic velocity scale of the representative eddy, and k_x and k_y are geometric constants where $k_x \ell$ and $k_y \ell$ are the average streamwise and spanwise spacings of the eddies in the plane of the wall. $\Delta(\overline{u_i u_j})$ corresponds to the stress contribution from one scale of packet-eddies and is defined as

$$\Delta(\overline{u_i u_j}) = \int_{-\infty}^{\infty} \int_{-\infty}^{\infty} \frac{\widetilde{U}_i \widetilde{U}_j}{U_0^2}\, d(x/\ell)\, d(y/\ell). \tag{B 2}$$

Similarly, the streamwise velocity deficit for all hierarchies can be computed by

$$\frac{U_\infty - \overline{U}}{U_\tau} = \frac{U_0}{k_x k_y} \int_{\delta_1}^{\delta} \Delta U_{eddy}(z/\ell)\, p_H(\ell)\, d\ell \tag{B 3}$$

where ΔU_{eddy} corresponds to the streamwise velocity contribution from one scale of representative packet-eddies and is defined as

$$\Delta U_{eddy} = \int_{-\infty}^{\infty} \int_{-\infty}^{\infty} \frac{\widetilde{U}}{U_0}\, d(x/\ell) d(y/\ell). \tag{B 4}$$

For this study, the velocity fields are scaled such that $\overline{uw}^+|_{peak} \approx 1$ in the log region, which has been empirically observed at sufficiently high Reynolds numbers. This provides us with an estimate of U_τ from (B 1) where

$$\frac{\overline{uw}^+|_{peak}}{U_\tau^2} = \frac{U_0^2}{k_x k_y} \underbrace{\int_{\delta_1}^{\delta} \Delta \overline{u_i u_j}|_{peak}\, p_H(\ell)\, d\ell}_{\mathscr{C}=\text{constant}} = 1, \tag{B 5}$$

and therefore

$$U_\tau^2 = \frac{k_x k_y}{\mathscr{C} U_0^2}\, \overline{uw}^+\bigg|_{peak}. \tag{B 6}$$

The estimate of U_τ from (B 6) can now be substituted into (B 1) to compute the other turbulence intensity components. This yields results which are independent of the population density parameters k_x and k_y, which cancel out. Conversely, when scaling the streamwise velocity deficit in (B 3) using the same estimate of U_τ, results are still dependent on k_x and k_y. Therefore, these parameters can be chosen such that the mean streamwise velocity profile in the logarithmic region satisfies

$$\frac{\overline{U}}{U_\tau} = \frac{1}{\kappa} \log(z^+) + A, \tag{B 7}$$

where $\kappa = 0.39$ (Kármán constant) and $A = 4.3$ (log-law intersect), following Marusic *et al.* (2013). However, in the present study we generate synthetic velocity fields consisting of randomly distributed packet-eddies rather than computing flow statistics from an integral form of a single representative packet-eddy ((B 1) and (B 3)). Consequently, the spatial population density (via k_x and k_y needs to be chosen appropriately to obtain the log-law constants ($\kappa \approx 0.39$ and $A \approx 4.3$), and this is done by adjusting the domain size occupied by the representative packet-eddies when generating the synthetic velocity fields.

REFERENCES

ACARLAR, M. S. & SMITH, C. R. 1987*a* A study of hairpin vortices in a laminar boundary. Part 1. Hairpin vortices generated by a hemisphere protuberance. *J. Fluid Mech.* **175**, 1–41.

ACARLAR, M. S. & SMITH, C. R. 1987*b* A study of hairpin vortices in a laminar boundary layer. Part 2. Hairpin vortices generated by fluid injection. *J. Fluid Mech.* **175**, 43–83.

ADRIAN, R. J. 2007 Hairpin vortex organization in wall turbulence. *Phys. Fluids* **19** (4), 041301.

ADRIAN, R. J. & MARUSIC, I. 2012 Coherent structures in flow over hydraulic engineering surfaces. *J. Hydraul Res.* **50** (5), 451–464.

ADRIAN, R. J., MEINHART, C. D. & TOMKINS, C. D. 2000 Vortex organization in the outer region of the turbulent boundary layer. *J. Fluid Mech.* **422**, 1–54.

ADRIAN, R. J. & WESTERWEEL, J. 2011 *Particle Image Velocimetry*. Cambridge University Press.

DEL ÁLAMO, J. C., JIMÉNEZ, J., ZANDONADE, P. & MOSER, R. D. 2004 Scaling of the energy spectra of turbulent channels. *J. Fluid Mech.* **500**, 135–144.

DEL ÁLAMO, J. C., JIMÉNEZ, J., ZANDONADE, P. & MOSER, R. D. 2006 Self-similar vortex clusters in the turbulent logarithmic region. *J. Fluid Mech.* **561**, 329–358.

BALTZER, J. R., ADRIAN, R. J. & WU, X. 2013 Structural organization of large and very large scales in turbulent pipe flow simulation. *J. Fluid Mech.* **720**, 236–279.

BLACKWELDER, R. F. & ECKELMANN, H. 1979 Streamwise vortices associated with the bursting phenomenon. *J. Fluid Mech.* **94** (03), 577–594.

CHAUHAN, K., PHILIP, J., DE SILVA, C. M., HUTCHINS, N. & MARUSIC, I. 2014 The turbulent/non-turbulent interface and entrainment in a boundary layer. *J. Fluid Mech.* **742**, 119–151.

CHAUHAN, K. A., MONKEWITZ, P. A. & NAGIB, H. M. 2009 Criteria for assessing experiments in zero pressure gradient boundary layers. *Fluid Dyn. Res.* **41** (2), 021404.

FALCO, R. E. 1977 Coherent motions in the outer region of turbulent boundary layers. *Phys. Fluids* **20**, S124–S132.

GANAPATHISUBRAMANI, B., LONGMIRE, E. K. & MARUSIC, I. 2003 Characteristics of vortex packets in turbulent boundary layers. *J. Fluid Mech.* **478**, 35–46.

HAMBLETON, W. T., HUTCHINS, N. & MARUSIC, I. 2006 Simultaneous orthogonal-plane particle image velocimetry measurements in a turbulent boundary layer. *J. Fluid Mech.* **560**, 53–64.

HEAD, M. R. & BANDYOPADHYAY, P. 1981 New aspects of turbulent boundary-layer structure. *J. Fluid Mech.* **107**, 297–338.

HERPIN, S., STANISLAS, M., FOUCAUT, J. M. & COUDERT, S. 2013 Influence of the Reynolds number on the vortical structures in the logarithmic region of turbulent boundary layers. *J. Fluid Mech.* **716**, 5–50.

HUTCHINS, N. & MARUSIC, I. 2007 Evidence of very long meandering features in the logarithmic region of turbulent boundary layers. *J. Fluid Mech.* **579**, 1–28.

JIMÉNEZ, J. 2012 Cascades in wall-bounded turbulence. *Annu. Rev. Fluid Mech.* **44**, 27–45.

KIM, K. C. & ADRIAN, R. J. 1999 Very large-scale motion in the outer layer. *Phys. Fluids* **11** (2), 417–422.

KLEWICKI, J. C. 2010 Reynolds number dependence, scaling, and dynamics of turbulent boundary layers. *Trans. ASME J. Fluids Engng* **132** (9), 094001.

KLEWICKI, J., EBNER, R. & WU, X. 2011 Mean dynamics of transitional boundary-layer flow. *J. Fluid. Mech.* **682**, 617–651.

KLINE, S. J., REYNOLDS, W. C., SCHRAUB, F. A. & RUNSTADLER, P. W. 1967 The structure of turbulent boundary layers. *J. Fluid Mech.* **30**, 741–773.

KWON, Y. S., MONTY, J. P., PHILIP, J., DE SILVA, C. M. & HUTCHINS, N. 2014 The quiescent core of turbulent channel flow. *J. Fluid Mech.* **751**, 228–254.

LEE, J., LEE, J. H., CHOI, J. & SUNG, H. J. 2014 Spatial organization of large- and very-large-scale motions in a turbulent channel flow. *J. Fluid Mech.* **749**, 818–840.

LEE, J. H. & SUNG, H. J. 2011 Very-large-scale motions in a turbulent boundary layer. *J. Fluid Mech.* **673**, 80–120.

MARUSIC, I. 2001 On the role of large-scale structures in wall turbulence. *Phys. Fluids* **13**, 735–743.

MARUSIC, I. 2009 Unravelling turbulence near walls. *J. Fluid Mech.* **630**, 1–4.

MARUSIC, I. & ADRIAN, R. J. 2012 The eddies and scales of wall turbulence. In *Ten Chapters in Turbulence* (ed. P. A. Davidson, K. Yukio & K. R. Sreenivasan). Cambridge University Press.

MARUSIC, I., MONTY, J. P., HULTMARK, M. & SMITS, A. J. 2013 On the logarithmic region in wall turbulence. *J. Fluid Mech.* **716**, R3.

MARUSIC, I. & PERRY, A. E. 1995 A wall-wake model for the turbulence structure of boundary layers. Part 2. Further experimental support. *J. Fluid Mech.* **298**, 389–407.

MEINHART, C. D. & ADRIAN, R. J. 1995 On the existence of uniform momentum zones in a turbulent boundary layer. *Phy. Fluids* **7**, 694.

MORRILL-WINTER, C. & KLEWICKI, J. 2013 Influences of boundary layer scale separation on the vorticity transport contribution to turbulent inertia. *Phys. Fluids* **25** (1), 015108.

NA, Y., HANRATTY, T. J. & LIU, Z. C. 2001 The use of DNS to define stress producing events for turbulent flow over a smooth wall. *Flow Turbul. Combust.* **66** (4), 495–512.

OFFEN, G. R. & KLINE, S. J. 1974 Combined dye-streak and hydrogen-bubble visual observations of a turbulent boundary layer. *J. Fluid Mech.* **62** (02), 223–239.

OFFEN, G. R. & KLINE, S. J. 1975 A proposed model of the bursting process in turbulent boundary layers. *J. Fluid Mech.* **70** (02), 209–228.

PERRY, A. E. & CHONG, M. S. 1982 On the mechanism of wall turbulence. *J. Fluid Mech.* **119**, 173–217.

PERRY, A. E., HENBEST, S. M. & CHONG, M. 1986 A theoretical and experimental study of wall turbulence. *J. Fluid Mech.* **165**, 163–199.

PERRY, A. E. & MARUSIC, I. 1995 A wall-wake model for the turbulence structure of boundary layers. Part 1. Extension of the attached eddy hypothesis. *J. Fluid Mech.* **298**, 361–388.

PHILIP, J., MENEVEAU, C., DE SILVA, C. M. & MARUSIC, I. 2014 Multiscale analysis of fluxes at the turbulent/non-turbulent interface in high Reynolds number boundary layers. *Phys. Fluids* **26** (1), 015105.

PRIYADARSHANA, P. J. A., KLEWICKI, J. C., TREAT, S. & FOSS, J. F. 2007 Statistical structure of turbulent-boundary-layer velocity–vorticity products at high and low Reynolds numbers. *J. Fluid Mech.* **570**, 307–346.

SCHLATTER, P., LI, Q., ÖRLÜ, R., HUSSAIN, F. & HENNINGSON, D. S. 2014 On the near-wall vortical structures at moderate Reynolds numbers. *Eur. J. Mech.* (B. *Fluids*) **48**, 75–93.

SILLERO, J. A., JIMÉNEZ, J. & MOSER, R. D. 2013 One-point statistics for turbulent wall-bounded flows at Reynolds numbers up to $\delta^+ = 2000$. *Phys. Fluids* **25** (10), 105102.

DE SILVA, C. M., GNANAMANICKAM, E. P., ATKINSON, C., BUCHMANN, N. A., HUTCHINS, N., SORIA, J. & MARUSIC, I. 2014*a* High spatial range velocity measurements in a high Reynolds number turbulent boundary layer. *Phys. Fluids* **26** (2), 025117.

DE SILVA, C. M., HUTCHINS, N. & MARUSIC, I. 2014*b* Regions of uniform streamwise momentum in turbulent boundary layers. In *19th Australasian Fluid Mechanics Conference*.

DE SILVA, C. M., MARUSIC, I., WOODCOCK, J. D. & MENEVEAU, C. 2015 Scaling of second- and higher-order structure functions in turbulent boundary layers. *J. Fluid Mech.* **769**, 654–686.

DE SILVA, C. M., PHILIP, J., CHAUHAN, K., MENEVEAU, C. & MARUSIC, I. 2013 Multiscale geometry and scaling of the turbulent–nonturbulent interface in high Reynolds number boundary layers. *Phys. Rev. Lett.* **111**, 044501.

SMITS, A. J., MCKEON, B. J. & MARUSIC, I. 2011 High-Reynolds number wall turbulence. *Annu. Rev. Fluid Mech.* **43**, 353–375.

THEODERSEN, T. 1952 Mechanism of turbulence. In *Proc. Mid-west. Conf. Fluid Mech.*

TOMKINS, C. D. & ADRIAN, R. J. 2003 Spanwise structure and scale growth in turbulent boundary layers. *J. Fluid Mech.* **490** (1), 37–74.

TOWNSEND, A. A. 1976 *The Structure of Turbulent Shear Flow*, 2nd edn. Cambridge University Press.

WALLACE, J. M., ECKELMANN, H. & BRODKEY, R. S. 1972 The wall region in turbulent shear flow. *J. Fluid Mech.* **54** (1), 39–48.

WESTERWEEL, J., FUKUSHIMA, C., PEDERSEN, J. M. & HUNT, J. C. R. 2005 Mechanics of the turbulent–nonturbulent interface of a jet. *Phys. Rev. Lett.* **95**, 174501.

WOODCOCK, J. D. & MARUSIC, I. 2015 The statistical behaviour of attached eddies. *Phys. Fluids* **27** (1), 015104.

WU, X. & MOIN, P. 2009 Direct numerical simulation of turbulence in a nominally-zero-pressure-gradient flat-plate boundary layer. *J. Fluid Mech.* **630**, 5–41.

ZHOU, J., ADRIAN, R. J., BALACHANDAR, S. & KENDALL, T. 1999 Mechanisms for generating coherent packets of hairpin vortices in channel flow. *J. Fluid Mech.* **387**, 353–396.